Nanoscale Advances

ROYAL SOCIETY OF CHEMISTRY

PAPER

View Article Online
View Journal | View Issue

Cite this: *Nanoscale Adv.*, 2023, **5**, 5122

Facile deposition of FeNi/Ni hybrid nanoflower electrocatalysts for effective and sustained water oxidation†

Muhammad Ali Ehsan,[a] Abuzar Khan,*[a] Munzir H. Suliman[a] and Mohamed Javid[b]

Bimetallic iron-nickel (FeNi) compounds are widely studied materials for the oxygen evolution reaction (OER) owing to their high electrocatalytic performance and low cost. In this work, we produced thin films of the FeNi alloy on nickel foam (NF) by using an aerosol-assisted chemical deposition (AACVD) method and examined their OER catalytic activity. The hybrid FeNi/Ni catalysts obtained after 1 and 2 h of AACVD deposition show improved charge transfer and kinetics for the OER due to the strong interface between the FeNi alloy and Ni support. The FeNi/Ni-2h catalyst has higher catalytic activity than the FeNi/Ni-1h catalyst because of its nanoflower morphology that provides a large surface area and numerous active sites for the OER. Therefore, the FeNi/Ni-2h catalyst exhibits low overpotentials of 300 and 340 mV at 50 and 500 mA cm^{-2} respectively, and excellent stability over 100 h, and ~0% loss after 5000 cycles in 1 M KOH electrolyte. Furthermore, this catalyst has a small Tafel slope, low charge transfer resistance and high current exchange density and thus surpasses the benchmark IrO_2 catalyst. The easy, simple, and scalable AACVD method is an effective way to develop thin film electrocatalysts with high activity and stability.

Received 8th May 2023
Accepted 22nd August 2023

DOI: 10.1039/d3na00298e

rsc.li/nanoscale-advances

1. Introduction

Hydrogen is gaining popularity as a renewable fuel because it has several advantages over traditional fossil fuels such as high energy density, CO_2 neutrality and environmental friendliness.[1–4] Among the various hydrogen production methods, electrochemical water splitting is one of the best ways to generate clean hydrogen with zero emissions and it can use other renewable energy sources such as solar panels or wind turbines, to provide the electricity needed.[5] It is well known that hydrogen production from water electrolysis is accompanied by the oxygen evolution reaction (OER), which determines the efficacy of the splitting process to achieve high hydrogen flux.[6] The slow kinetics of the OER remains a major concern, as it involves a complicated electron shifting process which needs extra energy to make oxygen and produce hydrogen on the counter electrode.[7] To compensate for the extra energy requirement, electrocatalysts with high conductivity and stability are recommended to be used to make the process economically viable.[8] For this purpose, noble metal-based catalysts such as IrO_2 and RuO_2 with optimal binding energy for the generated intermediates[9] are the state of the art catalysts for the OER and have been extensively investigated.[10,11] However, these catalysts are expensive owing to their low reserves and are unstable at high anodic potentials,[12] which undermine their importance for commercial scale utilization and for economical hydrogen production. As a result, much attention has been paid to the development of low cost and earth rich element electrocatalysts that can accelerate the reaction rate and increase the efficiency of the electrochemical process by lowering the overpotential requirement, hence making them suitable for practical applications.[13] Therefore, noble metal-free transition metal electro-catalysts have been extensively studied for the OER, but few of them could achieve simultaneously favorable activity and selectivity.[14] Among them, Ni, Co, Mo, and Fe based catalysts are more promising as they have moderate binding energy, next only to the noble metals, as indicated by the volcano plot.[15] Nickel based compounds have attracted a lot of attention and have been extensively applied in devices for energy generation[16] and storage,[17] because of their excellent electrical properties, low cost, and accessibility. A major challenge for the oxygen evolution reaction (OER) is the low conductivity and stability of Ni-based catalysts, which are widely used for this electrochemical process. To address this issue, Ni can be alloyed with other 3d transition metals, which can enhance the electronic and structural properties of the catalysts. This strategy can improve the OER performance by

[a]*Interdisciplinary Research Center for Hydrogen and Energy Storage (IRC-HES), Saudi Arabia. E-mail: abuzar@kfupm.edu.sa*

[b]*Core Research Facilities, King Fahd University of Petroleum & Minerals, Box 5040, Dhahran 31261, Saudi Arabia*

† Electronic supplementary information (ESI) available. See DOI: https://doi.org/10.1039/d3na00298e

modulating the spin state, coordination, oxidation, and bonding of the active sites. Alloying Ni with Fe has proven the best choice for developing highly active and stable electrocatalysts for water oxidation, which can outperform single-metal catalysts in terms of stability, activity, and selectivity.[18] Therefore, employing binary alloys of nickel with other noble and non-noble metals is a convincing strategy for increasing the catalytic OER performance at a reduced cost. The alloying of different metals can induce various effects, such as lattice strain, electronic structure modulation, ligand effect, ensemble effect, and synergistic effect, which can alter the adsorption and activation of reactants and intermediates on the catalyst surface. These effects can enhance or weaken the binding strength of certain species, thus tuning the catalytic activity and selectivity.[18] Moreover, the composition, size, and morphology of Ni–Fe electrocatalysts can also affect their catalytic properties by changing the surface area, exposed facets, and coordination environment of active sites.[19] Alloying causes multiple changes in the physical and chemical properties of metallic components which influence catalytic activity by ligand, ensemble, and strain effects. The ligand effect changes the electronic structure of metals by alloying. The ensemble effect changes the number of active sites by reducing the particle size. The strain effect changes the electronic structure of the surface by creating a lattice mismatch and hence can be utilized to design new and efficient catalysts.[20]

The incompletely filled 'd' orbital of Ni allows easy transfer of electrons and hence its alloys are expected to have high catalytic activity and potential for large-scale applications.[21] Nickel alloys with noble metals have been widely investigated due to their outstanding activity and stability as efficient electrocatalysts for water electrolysis.[22] Currently, research is focused on developing Ni alloy electrocatalysts with other non-noble metals such as Mo, Cr, Fe, *etc.*[23–25] Alloys of Ni and Fe are reported as the most promising electrocatalysts for oxygen evolution reactions due to their low cost, high activity, and stability.[23] Ni and Fe-based OER materials, including oxides, hydroxides, layered hydroxides, and alloys of binary and tertiary metal composites have been reported recently in several OER studies.[26–29] Notably, E. Hatami *et al.*[30] reported a novel Ni–Fe micro/nano urchin-like structure fabricated by a fast and one-step electrodeposition strategy which required overpotentials of only 292 and 374 mV to deliver 10 and 100 mA cm^{-2}. In another study,[31] a variant of the Fe–Ni catalyst developed on the carbon cloth support delivered a low overpotential of 290 mV with a Tafel slope of 51 mV dec^{-1} at a current density of 10 mA cm^{-2}. Similarly, various nickel–iron combinations have shown promising results for OER catalysis.[32,33] These studies have indicated that the catalyst fabrication process, morphology and support material are the important parameters which contribute towards higher efficiency of the OER. It has been observed that previous OER studies based on the NiFe electrocatalyst used nano powders, which certainly require some polymer binders (like Nafion) for better adhesion with the current collector. The addition of binder covers the active sites of the catalyst and causes its deactivation. Meanwhile, it increases the resistance between the catalyst and the current collector and hinders the easy transfer of electrons, thereby deteriorating the conductivity. Moreover, such bonded catalysts are not mechanically stable, and the catalyst easily flakes off under severe oxygen evolution conditions, particularly when higher current densities are applied.[34] These issues need to be solved to understand the full potential of nanostructured catalysts. Therefore, by developing a polymeric binder-less electrocatalytic thin film, higher conductivity can be achieved, resulting in improved electrocatalytic activity.

In the current work, we have developed an iron-nickel (FeNi) alloy catalyst directly on nickel foam (NF) by following a thin film deposition process based on aerosol assisted chemical vapor deposition (AACVD). AACVD is a custom designed, inexpensive, and single step thin film fabrication process which can create nanomaterials directly on a support surface without any need of binder or reagent to bind the catalyst with the support. As the catalyst is directly developed over the support surface, the inherent conductivity of the catalyst is retained. Moreover, the nano morphologies can be easily controlled with the deposition parameters such as deposition time, temperature, and nature of solvent. Thus, porous Fe–Ni thin alloy film catalysts produced on nickel foam for time periods of 1 h and 2 h have been investigated for the OER. The FeNi catalyst grown for 2 h initiated water oxidation at 1.4 V *vs.* RHE (=170 mV) and achieved current densities of 50 and 500 mA cm^{-2} by consuming overpotentials of 300 and 340 mV respectively. Moreover, the catalyst remained stable for over 100 h under the continuous water oxidation operation performed at varying current densities. The catalyst outperformed the benchmark IrO_2/NF catalyst when tested for the OER under similar conditions. The competitive activity and outstanding durability of the FeNi/Ni alloy catalyst demonstrate its great ability to replace precious metal catalysts in future practical applications.

2. Experimental

2.1 Chemicals and materials

The study used the following chemicals: iron(III) acetylacetonate ($Fe(acac)_3$), nickel(II) acetylacetonate ($Ni(acca)_2$), and methanol purchased from Sigma-Aldrich. Nickel foam (1.6 mm thick and 95% porosity) was purchased from Good-fellow Cambridge Ltd. The water used throughout all experiments was Milli-Q water.

2.2 Synthesis of FeNi thin alloy films

The nickel foam (NF) strips of size (1 cm × 2 cm) were precleaned with diluted HCl, acetone and ethanol for 10 min each in an ultrasonic bath. Then, the NF was rinsed with deionized water and blown with high-purity N_2 gas.

The iron–nickel alloy (FeNi) thin film electrocatalyst was developed on Ni foam using an in-house built aerosol-assisted chemical vapor deposition (AACVD) strategy. The schematic presentation of AACVD and its operational details have been described in our earlier work. The solution of the dual precursor of $Fe(acac)_3$ (100 mg, 0.283 mmol) and $Ni(acac)_2$ (73 mg, 0.283 mmol) was prepared in 15 mL of methanol. The aerosol mist from the dual precursor solution was produced using an

ultrasonic humidifier, and a mist stream was transferred to a horizontal tube furnace preheated at 475 °C with the help of carrier gas (10% H_2 + 90% N_2). The NF in the tube furnace was positioned to receive the precursor nebula directly over it, where the decomposition of the precursor and CVD reactions took place to develop a layer of FeNi material. The deposition process was repeated for a period of 1 h and 2 h, respectively and the prepared samples were named as FeNi/Ni-1h and FeNi/Ni-2h, respectively. After completing the deposition experiments, the aerosol supply was closed and 100% H_2 gas was passed over the catalyst films to ensure the FeNi alloy formation. The amount of the deposited FeNi alloy on NF was obtained from the difference in the weight of NF before and after deposition. The amount of the FeNi alloy on FeNi/Ni-1h and FeNi/Ni-2h was found to be 47 μg and 88 μg respectively.

2.3 Structural characterization

The catalyst morphology was seen with a scanning electron microscope (SEM) JEOL JSM-6610LV (Japan). An energy-dispersive X-ray spectrometer (EDX, INCA Energy 200, Oxford Instruments, UK) was used to find the elemental composition of the catalyst. The crystalline structure was recorded by X-ray diffraction (XRD, Rigaku MiniFlex X-ray diffractometer (Japan)), which was used to measure the crystalline pattern of the films over a 2θ range of 20–90°. The TEM measurement analysis was performed using a JEOL-JEM2100F, Japan, operating at an acceleration voltage of 200 kV. X-ray photoelectron spectroscopy (XPS, Thermo Scientific EscaLab 250Xi, USA) with an Al Kα (1486.6 eV) source was performed to examine the chemical composition and valence states. The electron beam was calibrated with C 1s (284.6 eV) as the standard.

2.4 Electrochemical measurements

A computer controlled Autolab potentiostat workstation with the Nova 2.1.6. Interface was used to investigate the electrocatalytic water oxidation by FeNi/Ni film electrodes. We set up a typical three-electrode cell with platinum (Pt) rod, Ag/AgCl, and FeNi film electrodes as the counter, reference, and working electrodes, respectively. The electrochemical tests were conducted in 1.0 M KOH electrolyte and the potential readings were converted to the reversible hydrogen electrode (RHE) scale. To activate the catalyst surface for water oxidation, cyclic voltammetry (CV) analysis in the potential range of 1–2 V (*vs.* RHE) was performed. The linear sweep voltammetry (LSV) test at a scan rate of 5 mV s^{-1} was carried out and data were reported with *iR* corrections. Electrochemical impedance spectroscopy (EIS) at a potential of 1.50 V in the frequency range from 0.01 Hz to 100 kHz was performed. The long-term catalytic durability was evaluated using the chronopotentiometry (CP) method for a period of 100 h. The *iR* drop was corrected using the following formula:

$V' = iR$; where V' is the *iR*-corrected potential, and i is the value of current obtained from the CV and LSV measurements. R_s is the value of solution resistance obtained from the EIS measurement after electrochemical fitting. The solution resistance was determined by fitting the high-frequency region of the EIS data with an equivalent circuit. The *iR* correction was performed after the CV and LSV measurements were completed. The *iR*-corrected data were then used for further analysis.

3. Results and discussion

3.1 Structure and morphology

The iron-nickel (FeNi) alloy films were fabricated for time periods of 1 and 2 h using an AACVD approach. Fig. 1 shows the XRD patterns of obtained FeNi alloy films on plain glass. The obvious peaks at 2θ of 45°, 52.3° and 76.7° result from the reflection planes of (111), (200) and (220), respectively and correspond to the bulk nickel (PDF: 077-8341). The characteristic Fe peaks are missing owing to the formation of the Fe–Ni alloy. From Fig. 1 it is noted that the XPD peaks of standard "Ni" are slightly shifted to a higher 2θ value in the case of Fe–Ni samples, which could be attributed to the lattice narrowing when the Ni atoms are replaced by Fe atoms with a smaller radius. A similar observation is reported by Z. Zhang *et al.* for the Fe–Ni alloy electrocatalyst prepared by a one-step potentiostatic electrodeposition method.[35]

Fig. 2 shows the SEM morphology of the FeNi alloy catalyst produced on nickel foam as a result of 1 and 2 h deposition *via* AACVD. The FeNi/Ni-1h alloy shows the formation and distribution of small sized crystallites over a large area of NF struts (Fig. 2a). The design, shape and texture of these crystallites become visible in a high-magnification image, which exhibits a blooming flower-like pattern with regularly interconnected petal features. The direct deposition for 2 h developed a significantly large and thick plant-like object and its corresponding high-magnification image clearly shows the vertically aligned petals which are stacked together to create another flower pattern. The development of hierarchical flower like structures in both catalyst samples seems fluffy and porous presenting a high surface area with uniform distribution of catalytically active sites. The 3D NF with hierarchical and porous petal networks offers a promising platform for various applications such as water splitting, supercapacitors, and hydrogen

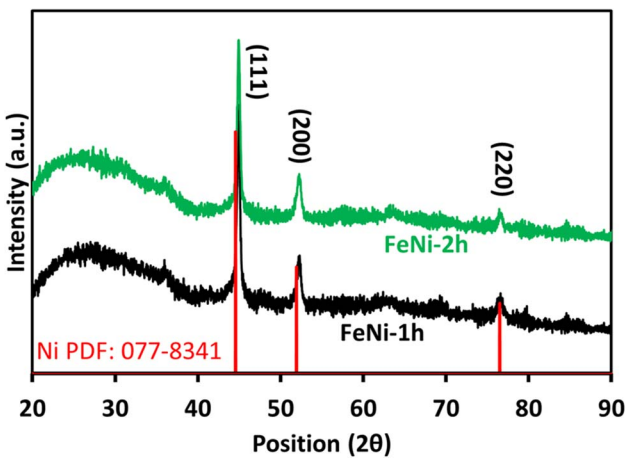

Fig. 1 XRD patterns of iron-nickel (Fe–Ni) alloy films grown on plain glass for periods of 1 and 2 h *via* AACVD.

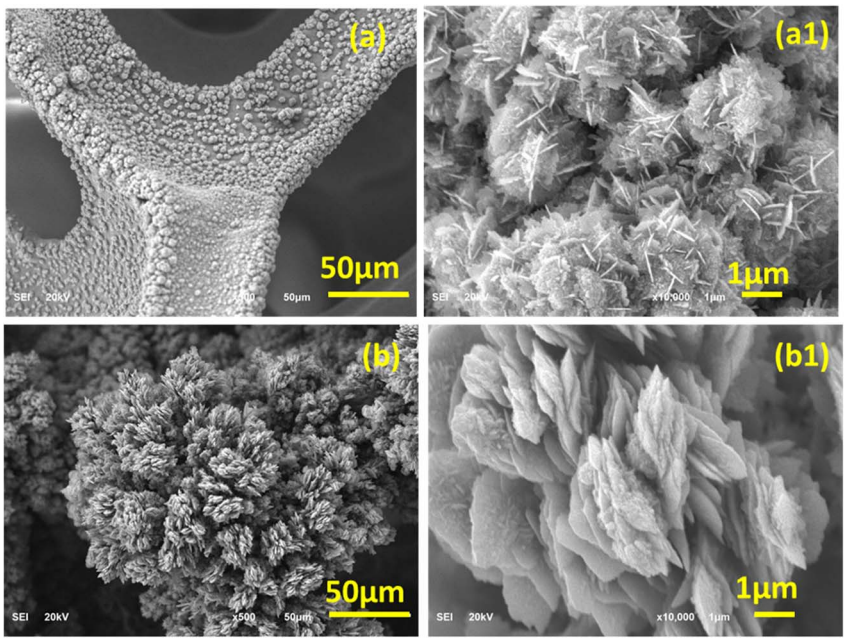

Fig. 2 SEM morphologies of FeNi alloy catalysts deposited on the nickel foam substrate for different time periods; (a and a1) 1 h and (b and b1) for 2 h. (a and b) at 50 µm scale and (a1 and b1) at 1 µm.

storage.[25,36–38] The petal networks facilitate the contact between the electrolyte ions and the catalyst material. The FeNi petals synthesized after 2 h of deposition time have more active centers at the surface that can enhance the OER performance. These active centers are influenced by the surface structure, nanoparticle shape/size and the electrolyte composition.

The elemental composition of the FeNi alloy catalyst was investigated by EDX analysis. For this, the catalyst film prepared on a plain glass was used to avoid the addition of Ni from the nickel foam substrate, which might otherwise increase the concentration of Ni present in the as-synthesized catalyst samples. The presence of Fe and Ni elements suggests the synthesis of FeNi catalysts, and the Au peaks are attributed to the gold coating used to avoid the charging effect under SEM. The percent (%) atomicity in the FeNi alloy catalyst is found to be 47.6/52.4 and 48.3/51.7 representing an empirical elemental ratio between Fe : Ni atoms, which is nearly 1 to 1. The absence of the oxygen (O) element indicates the synthesis of the pure alloy material. Additionally, the EDX map analysis (Fig. S1†) confirmed that Fe and Ni atoms are homogenously and uniformly distributed in the alloy materials.

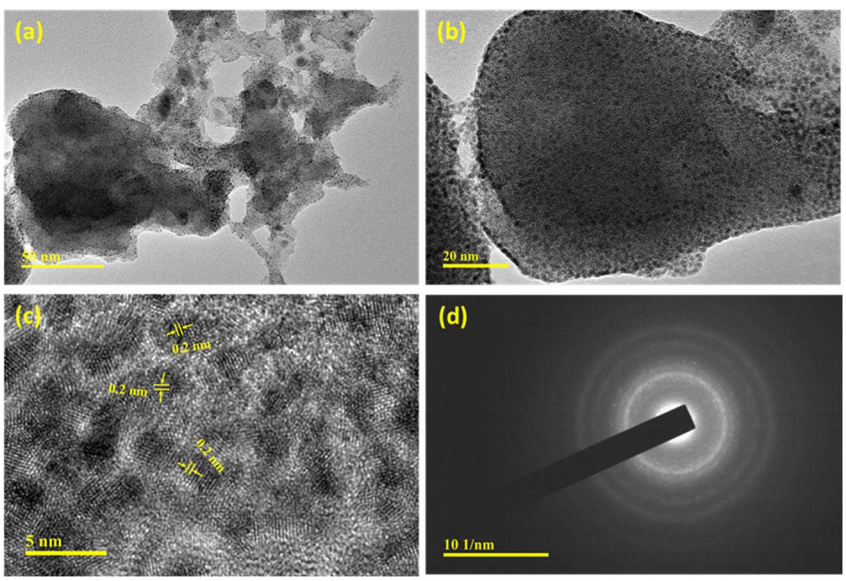

Fig. 3 TEM analysis of the FeNi/Ni-2h alloy catalyst: (a) low-resolution and (b) high resolution TEM images. (c) HR-TEM at 5 nm presenting the lattice fringes of Ni. (d) SAED showing the ring formation for a polycrystalline nature of Ni.

The nanostructure of the FeNi/Ni-2h catalyst was further analyzed by TEM analysis (Fig. 3). The nano-sheet like morphology found in TEM images (Fig. 3a and b) indicates a good correlation with the SEM result. The TEM images show the presence of quantum dots of size 2–4 nm inside these nanosheets. Although it is hard to identify Fe and Ni atoms, the value of the characteristic spacing is 0.20 nm,[39] corresponding well to the high intensity (111) crystal facet of metallic nickel as observed in XRD data. Furthermore, the selected area electron diffraction pattern (SAED) (Fig. 3d) shows the formation of symmetrical rings demonstrating the poly-crystalline nature of the FeNi alloy catalyst.

3.2 Electrochemical properties of FeNi thin films

The OER characteristics of the FeNi electrocatalyst were investigated by assembling a three-electrode cell connected with a potentiostat in 1.0 M KOH electrolyte. Initially, the catalytic films were activated by conducting a concurrent cyclic

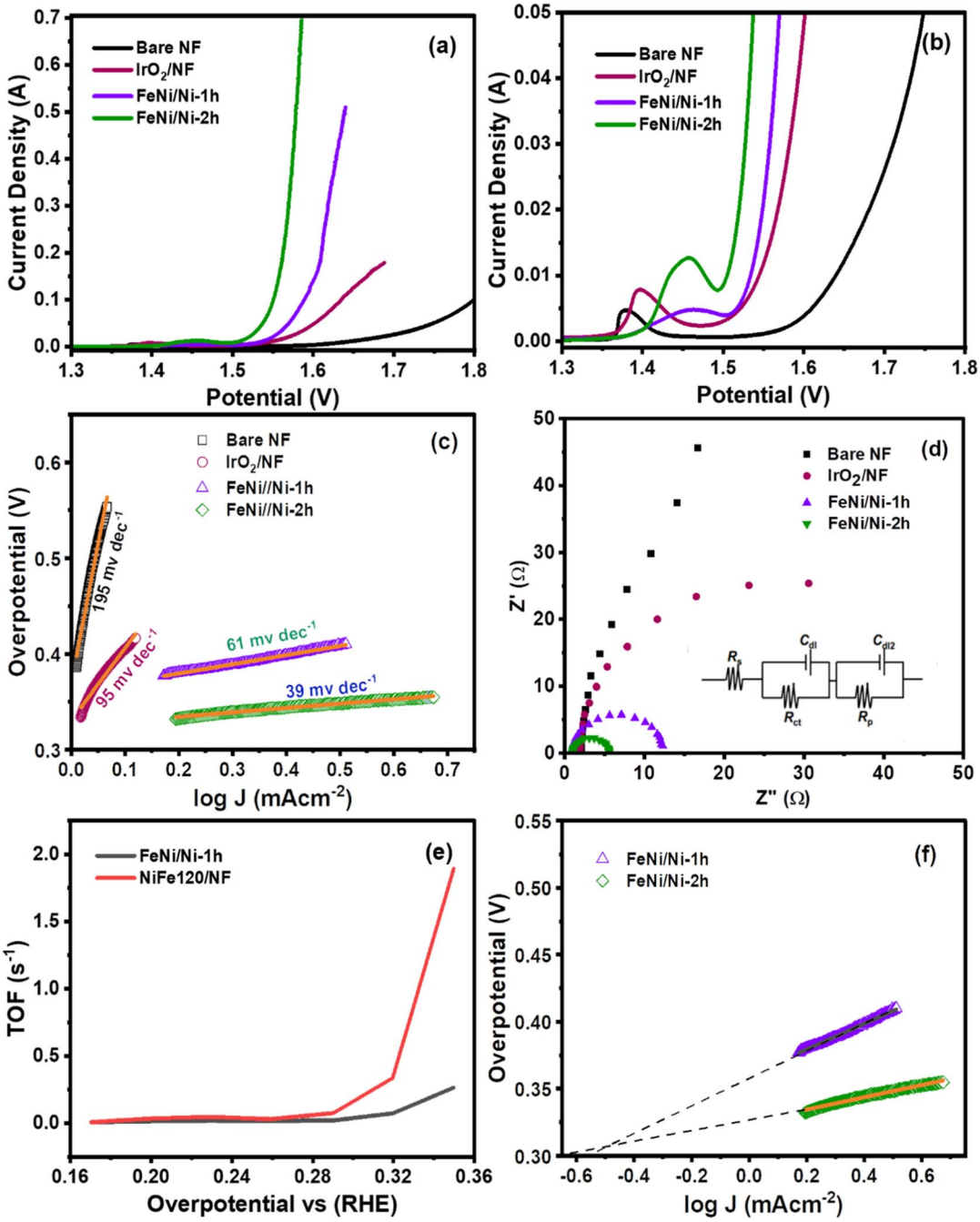

Fig. 4 Electrocatalytic investigations; (a) polarization curves at a scan rate of 5 mV s^{-1} in 1.0 M KOH electrolyte solution for FeNi catalysts deposited over NF at various deposition times; (b) zoomed view of polarization curves (c) Tafel slope; (d) Nyquist plots for FeNi catalysts compared with bare NF and IrO_2/NF; (e) TOF values of all catalytic systems (recorded at various potentials directly from polarization curves) investigated in this study; (f) current exchange density.

Table 1 The EIS parameters of NF, IrO_2, FeNi/Ni-1h and FeNi/Ni-2h

Electrocatalyst	R_s	R_p	R_{ct}
NF	2.1	22.2	2.10×10^4
IrO_2	1.9	0.11	51
FeNi/Ni-1h	0.85	0.1	11.4
FeNi/Ni-2h	1	1.8	2.8

voltammetry (CV) test, which promotes active species on the surface of the catalyst. The results of 25 continuous CV scans of both FeNi catalysts are shown in Fig. S2.† The shape and features of the CVs revealed valuable information about the kinetics and mechanisms of the electrochemical reactions occurring at the electrode–electrolyte interface. In the CV plot, forward biasing produces an anodic peak in the region 1.4–1.5 V which suggests the conversion of metallic species into high valent species *i.e.*, oxide/oxyhydroxide species which are more active for breaking the hydroxyl ion (OH^-) to produce oxygen. A slight variation in the oxidation peak position might be due to the composition and structure of the FeNi alloys, as well as the electrolyte conditions.[40] Several possible explanations have been proposed for this shift in the anodic peak such as (i) formation of a metastable FeNi oxyhydroxide phase, which has a higher oxidation potential than NiOOH. (ii) The incorporation of Fe into the NiOOH lattice, which modifies its electronic structure and catalytic properties. (iii) The dissolution and re-deposition of Fe species from the electrolyte, which affect the surface morphology and composition of the FeNi alloys.[41] As the CV progresses, the oxidation peak area becomes wider which suggests that *in situ* formation of catalytic species is increasing.

After surface activation and stabilization of the fabricated electrocatalysts, their OER performance was evaluated and compared using linear sweep voltammetry (LSV) performed in 1.0 M KOH solution at a scan rate of 5 mVs^{-1}. For comparison, bare NF and IrO_2 coated NF were also tested under similar conditions. Fig. 4a shows the polarization curves of all catalytic systems. Apparently, in all catalytic systems, the current density peak rapidly increases after 1.5 V. The comparative LSV curves clearly show that both FeNi/Ni-1h and FeNi/Ni-2h have better OER performance when compared with IrO_2/NF and bare NF. Particularly, FeNi/Ni-2h reaches a maximum current density of 700 mA cm^{-2} at 1.57 V, while FeNi/Ni-1h only reaches a current density of 500 mA cm^{-2} at a higher potential of 1.65 V, indicating a faster heterogeneous electron transfer process in the FeNi/Ni-2h catalyst. The benchmark IrO_2 and bare nickel foam exhibit higher potentials and lower peak current densities compared to both FeNi catalysts. Fig. 4b presents the enlarged view of these LSV curves, which clearly show that water oxidation in the FeNi/Ni-2h catalyst begins a bit earlier (at 1.47 V η_{onset} = 240 mV) than that in the FeNi/Ni-1h catalyst (1.53 V η_{onset} = 300 mV), while both catalysts maintained a potential difference ($\Delta\eta$) of 40 mV to reach a current density of 50 mA cm^{-2}. Nevertheless, to reach a current density of 50 mA cm^{-2}, the FeNi/Ni-1h catalyst requires an overpotential of 340 mV which is less than that of the benchmark IrO_2 (370 mA).

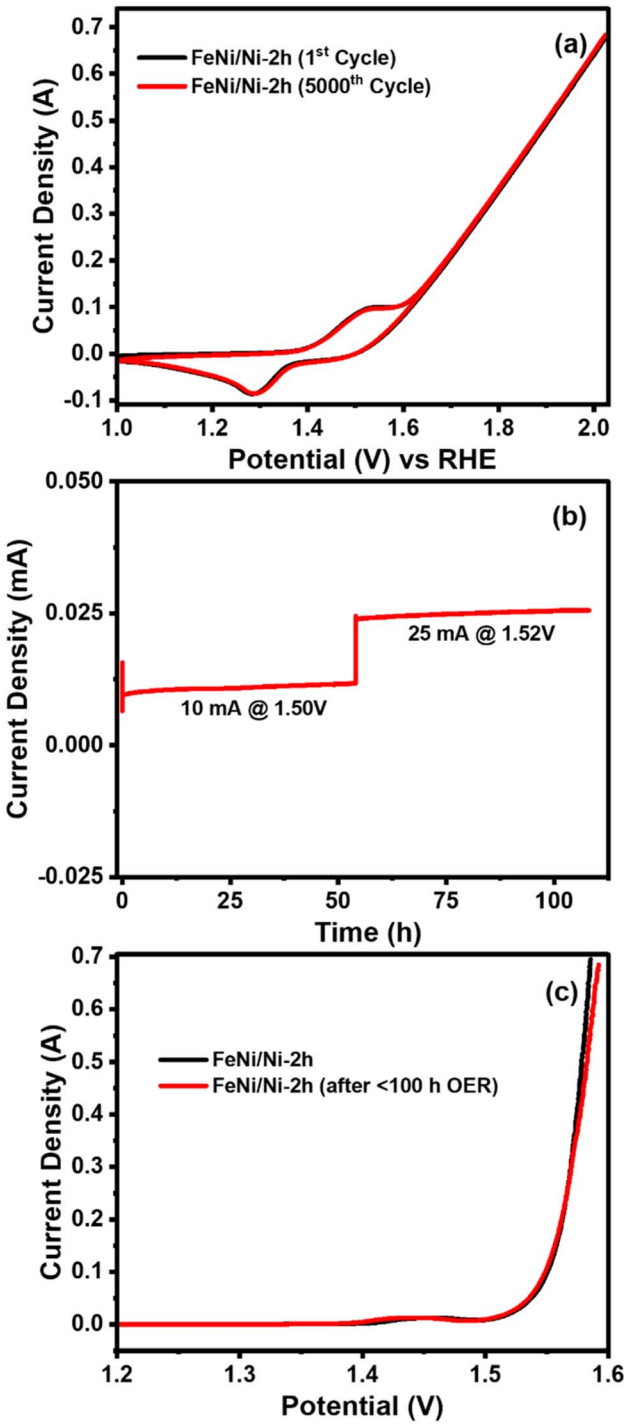

Fig. 5 (a) CV test of FeNi/Ni-2h for 5000 cycles @ scan rates of 50 mV s^{-1} in 1.0 M KOH electrolyte solution; (b) chronoamperometry response (η *vs.* *t*) of the FeNi/Ni-2h catalyst at two different applied current densities of 10 and 25 mA cm^{-2} in 1.0 M KOH electrolyte solution; (c) polarization curves of the FeNi/Ni-2h catalyst before and after the chronoamperometry experiment.

Further, the Tafel slope has been extracted from the polarization curves to compare the OER kinetics of different catalysts involved in this study. The Tafel equation: $\eta = a + b \log j$ is used to fit the linear part of the Tafel curve and Fig. 4c shows that

FeNi/Ni-2h has the lowest Tafel slope value of 39 mV dec^{-1} followed by FeNi/Ni-1h (69 mV dec^{-1}) IrO_2 (95 mV dec^{-1}) and bare NF (195 mV dec^{-1}). The smaller Tafel value of the FeNi/Ni-2h catalyst indicates its ability to transfer charge at faster rates than the other catalysts, and thus it shows superior OER activity to FeNi alloy catalysts indicating a higher OER kinetics on the FeNi surface.

A further insight into electrocatalyst kinetics is obtained through electrochemical impedance spectroscopy (EIS) which describes about the electrical resistance and interfacial charge transfer resistance (R_{ct}) between the surface of an electrode and H_2O/OH. The electrical conductivity of an electrode is a crucial factor that modifies its efficacy. Typically, higher electrical conductivity results in a quicker charge transfer and consequently greater performance. Fig. 4d depicts the EIS Nyquist plots of all electrocatalysts (NF, IrO_2, FeNi/Ni-1h, and FeNi/Ni-2h) recorded at a potential of 1.5 V_{RHE}. The resistance or kinetics of interfacial charge transfer near the electrode surface can be inferred from the semicircular dispersion in Nyquist plots. The semicircular arcs represent the frequency response of the transfer function in Cartesian coordinates. The smaller the arc, the lower the resistance or faster the charge transfer. A two-time constant parallel model was used to fit all EIS data, based on the Nyquist analysis that showed the existence of a circuit with two-time constants. This model consists of R_s in series with two parallel constant phase element-resistance. The R_s represents collective resistances, including wiring resistance (R_{wiring}) and solution resistance (R_{solu}). In addition, R_{ct} and R_p represent, respectively,[42,43] (summarized in Table 1) the charge transfer resistance and surface (porous or irregular texture) resistance. The FeNi/Ni-2h catalyst demonstrates the lowest R_{ct} value and hence better charge transport and conductivity as compared to the other electrocatalysts.

In addition, the inherent catalytic activity of both FeNi electrocatalysts was assessed by measuring the turnover frequency (TOF) using the following formula:

$$\mathrm{TOF} = \frac{j \times A}{4 \times F \times m}$$

where j stands for the current density, A is the geometric surface area (1 cm^2) of the NF substrate, F is the Faraday constant of value 96 485 C mol^{-1}, and m is the number of moles of catalyst that have been deposited on the NF substrate.[42,44] Fig. 4e indicates the TOF plot of the FeNi electrocatalysts measured at various overpotentials. The FeNi/Ni-1h and FeNi/Ni-2h electrocatalysts exhibit TOF values of 0.25 s^{-1} and 1.85 s^{-1}, respectively at an overpotential of 350 mV. The FeNi/Ni-2h electrode has a significantly larger TOF value than its analog (NiFe-1h), which reveals its highly conducting nature and superior OER activity. The intrinsic electrocatalytic activity was further evaluated by studying the exchange current density (J_0). The exchange current density reflects the electron transfer ability of the catalyst material. Electrocatalysts with higher current density need less driving force to drive the charges. The exchange current density is obtained by extending the linear part of the Tafel curve to the X-axis (Fig. 4f). At zero over potential, the log [j] values of FeNi/Ni-1h and FeNi/Ni-2h are found to be 0.044 and 0.65 which correspond to the J_0 values of 2.7 and 4.4 mA cm^{-2}, respectively. Again, the higher exchange current density of the FeNi/Ni-2h catalyst makes it remarkable for OER catalysis.

Besides higher electrocatalytic activity, long term OER stability is another important factor which decides the suitability of a catalyst for practical demonstration. The FeNi/Ni-2h catalyst was subjected to prolonged OER measurements by two different kinds of tests. First, the catalyst was subjected to a continuous CV run for 5000 cycles and the results of the 1st and 5000th cycles are compared in Fig. 5a which have the same profile. After CV, the chronopotentiometric (CP) test for more than 100 h was carried out by applying two potentials of 1.50 and 1.52 V, respectively to observe the corresponding current profiles displayed in Fig. 5b, which shows a linear behavior. Both stability tests (CV and CP) show the high stability and endurance of the FeNi electrocatalyst under rigorous OER conditions. Right after CP measurement, the polarization curve was measured again and compared with its response before the stability test as shown in Fig. 5c. The polarization curve after the stability test is consistent with its initial behavior.

In order to investigate the compositional change in the FeNi/Ni-2h catalyst as a result of 100 h of chronopotentiometric testing, EDX analysis was conducted. Fig. S3† indicates the EDX spectrum which reveals the presence of mandatory Fe and Ni atoms on the surface of the catalyst. However, the concentration of oxygen, which was completely absent before the OER

Table 2 Comparison of different Fe–Ni bimetallic electrocatalysts for the OER in 1 M KOH

Catalyst/system	Support	Synthetic strategy	Potential [mV] @ 50 mA cm^{-2}	Peak current density [mA cm^{-2}]	Tafel slope [mV dec^{-1}]	Ref.
FeNi-2h	NF	AACVD	300	<700	39	This work
Ni–Fe–P	NF	Electrodeposition	330	~140	69	45
$Fe_{0.4}Ni_{0.6}$ alloy	NF	Heat treatment process	300	120	67	46
Fe–Ni–O_x NPs	NF	Aerosol spray approach	315	>80	38	47
Ni–Fe alloy	Cu foil	Electrodeposition	325	350	86	30
$(Ni_{0.5}Fe_{0.5})_2P$	GC	Ketjenblack carbon (KB)-templated	~380	120	77	48
NiFeOOH	GC	Electrodeposition	375	50	NA	49
Metallic Ni thin film	NF	AACVD	310	>700	73	44
IrO_2	Glassy carbon	Commercial	301	>170	75	50
RuO_2	NF	Commercial	322	400	55	51

(Fig. S1†), has significantly increased after long term OER. The presence of oxygen suggests the formation of $NiFeO_x$ due to the occurrence of oxidation reaction.

The influential OER performance of the FeNi alloy thin film electrocatalyst can be attributed to the following factors: (i) the use of a suitable deposition method based on AACVD to develop FeNi thin films directly on the nickel foam support resulted in a robust electrocatalyst which enhanced the electrical conductivity of the catalyst, (ii) the 2 h deposition yielded a highly porous nanoflower structure providing abundantly available catalytically active sites to facilitate improved reaction kinetics, and (iii) the porosity and 3-D texture of Ni-foam as a support allow penetration, increase electron/ion transport paths, and excessively disperse the electroactive phase.

Finally, Table 2 compares the key water oxidation parameters of different types of bimetallic Fe–Ni electrocatalysts prepared by different methods on different substrates. The FeNi alloy film catalyst prepared for 2 h by the AACVD process clearly shows a lower overpotential and has a tendency to produce a higher current density of <700 mA cm^{-2} as compared to the other electrocatalysts.

4. Conclusions

In this research paper, we have demonstrated the synthesis of thin films of the FeNi alloy on nickel foam using an aerosol-assisted chemical deposition (AACVD) method and their application as efficient electrocatalysts for the oxygen evolution reaction (OER). We have shown that the thin films of the FeNi alloy form hierarchical flower-like structures with a high surface area and uniform distribution of catalytically active sites. The TEM images reveal the presence of quantum dots of size 2–4 nm inside these nanosheets, which are attributed to the high intensity (111) crystal facet of metallic nickel. The FeNi/Ni-2h catalyst exhibits superior OER performance with low overpotentials, excellent stability, and high turnover frequency (TOF) values compared to other catalysts. The enhanced OER activity of the FeNi/Ni-2h catalyst is attributed to its highly conducting nature, faster charge transfer, and synergistic effect of Fe and Ni atoms. Our findings suggest that the AACVD method is a simple and effective way to produce thin films of the FeNi alloy with desirable morphology and structure for OER catalysis. This work provides a new insight into the design and optimization of metal alloy-based electrocatalysts for water splitting applications.

Conflicts of interest

The authors declare no conflict of interest.

Acknowledgements

The authors acknowledge the Interdisciplinary Research Center for Hydrogen and Energy Storage (IRC-HES) and the project INHE 2310 at King Fahd University of Petroleum and Minerals (KFUPM) for supporting this research work.

References

1 M. Ziegler, *MTZ Worldwide*, 2023, **84**, 24–27.
2 K. Mazloomi and C. Gomes, *Renewable Sustainable Energy Rev.*, 2012, **16**, 3024–3033.
3 Z. Abdin, A. Zafaranloo, A. Rafiee, W. Mérida, W. Lipiński and K. R. Khalilpour, *Renewable Sustainable Energy Rev.*, 2020, **120**, 109620.
4 M. Momirlan and T. N. Veziroglu, *Int. J. Hydrogen Energy*, 2005, **30**, 795–802.
5 L. Gao, X. Cui, C. D. Sewell, J. Li and Z. Lin, *Chem. Soc. Rev.*, 2021, **50**, 8428–8469.
6 G. Liu, K. Dastafkan and C. Zhao, *Heterog. Catal.*, 2021, 533–555.
7 B. You and Y. Sun, *Acc. Chem. Res.*, 2018, **51**, 1571–1580.
8 F. M. Sapountzi, J. M. Gracia, C. J. K. J. Weststrate, H. O. A. Fredriksson and J. W. H. Niemantsverdriet, *Prog. Energy Combust. Sci.*, 2017, **58**, 1–35.
9 J. Zhao, J.-J. Zhang, Z.-Y. Li, X.-H. Bu, J. Zhao, J.-J. Zhang, Z.-Y. X. Li, -H. Bu and -H. X. Bu, *Small*, 2020, **16**, 2003916.
10 C. Ma, W. Sun, W. Qamar Zaman, Z. Zhou, H. Zhang, Q. Shen, L. Cao and J. Yang, *ACS Appl. Mater. Interfaces*, 2020, **12**, 34980–34989.
11 L. Zhang, H. Jang, H. Liu, M. G. Kim, D. Yang, S. Liu, X. Liu and J. Cho, *Angew. Chem.*, 2021, **133**, 18969–18977.
12 M. Schalenbach, O. Kasian, M. Ledendecker, F. D. Speck, A. M. Mingers, K. J. J. Mayrhofer and S. Cherevko, *Electrocatalysis*, 2018, **9**, 153–161.
13 Y. Yang, X. Cui, D. Gao, H. He, Y. Ou, M. Zhou, Q. Lai, X. Wei, P. Xiao and Y. Zhang, *Sustainable Energy Fuels*, 2020, **4**, 3647–3653.
14 S. Dou, X. Wang, S. Wang, S. Dou, S. Wang and X. Wang, *Small Methods*, 2019, **3**, 1800211.
15 E. Fabbri, A. Habereder, K. Waltar, R. Kötz and T. J. Schmidt, *Catal. Sci. Technol.*, 2014, **4**, 3800–3821.
16 S. Bepari and D. Kuila, *Int. J. Hydrogen Energy*, 2020, **45**, 18090–18113.
17 L. Zhang, D. Shi, T. Liu, M. Jaroniec and J. Yu, *Mater. Today*, 2019, **25**, 35–65.
18 M. Du, X. Li, H. Pang and Q. Xu, *EnergyChem*, 2023, **5**, 100083.
19 L. Gao, X. Cui, Z. Wang, C. D. Sewell, Z. Li, S. Liang, M. Zhang, J. Li, Y. Hu and Z. Lin, *Proc. Natl. Acad. Sci. U. S. A.*, 2021, **118**(7), e2023421118.
20 J. Fan, H. Du, Y. Zhao, Q. Wang, Y. Liu, D. Li and J. Feng, *ACS Catal.*, 2020, **10**, 13560–13583.
21 W. M. H. Sachtler and P. Van Der Plank, *Surf. Sci.*, 1969, **18**, 62–79.
22 N. U. A. Babar, A. Khan, M. H. Suliman, M. A. Marwat, M. Nawaz Tahir and M. A. Ehsan, *Energy Fuels*, 2022, **36**, 5910–5919.
23 J. Zhao, J.-J. Zhang, Z.-Y. Li, X.-H. Bu, J. Zhao, J.-J. Zhang, Z.-Y. X. Li, -H. Bu and -H. X. Bu, *Small*, 2020, **16**, 2003916.
24 M. Qin, G. Ma, Z. Fan, Y. Chen and X. Xin, *New J. Chem.*, 2023, **47**, 596–602.
25 M. A. Ehsan and A. Khan, *ACS Omega*, 2021, **6**, 31339–31347.

26 M. Wang, Y. Wang, S. S. Mao and S. Shen, *Nano Energy*, 2021, **88**, 106216.
27 M. Gao, W. Sheng, Z. Zhuang, Q. Fang, S. Gu, J. Jiang and Y. Yan, *J. Am. Chem. Soc.*, 2014, **136**, 7077–7084.
28 M. Gong, Y. Li, H. Wang, Y. Liang, J. Z. Wu, J. Zhou, J. Wang, T. Regier, F. Wei and H. Dai, *J. Am. Chem. Soc.*, 2013, **135**, 8452–8455.
29 K. L. Nardi, N. Yang, C. F. Dickens, A. L. Strickler, S. F. Bent, K. L. Nardi, C. F. Dickens, A. L. Strickler, S. F. Bent and N. Yang, *Adv. Energy Mater.*, 2015, **5**, 1500412.
30 E. Hatami, A. Toghraei and G. Barati Darband, *Int. J. Hydrogen Energy*, 2021, **46**, 9394–9405.
31 H. Zhong, T. Liu, S. Zhang, D. Li, P. Tang, N. Alonso-Vante and Y. Feng, *J. Energy Chem.*, 2019, **33**, 130–137.
32 T. S. Munonde and H. Zheng, *Ultrason. Sonochem.*, 2021, **76**, 105664.
33 B. Buccheri, F. Ganci, B. Patella, G. Aiello, P. Mandin and R. Inguanta, *Electrochim. Acta*, 2021, **388**, 138588.
34 Q. Wang, Y. Cheng, H. B. Tao, Y. Liu, X. Ma, D. S. Li, H. Bin Yang and B. Liu, *Angew. Chem., Int. Ed.*, 2023, **62**, e202216645.
35 Z. Zhang, Y. Wu and D. Zhang, *Int. J. Hydrogen Energy*, 2022, **47**, 1425–1434.
36 J. Choi, A. Nkhama, A. Kumar, S. R. Mishra, F. Perez and R. K. Gupta, *Int. J. Hydrogen Energy*, 2022, **47**, 7511–7521.
37 X. Xu, T. Wang, M. Zheng, Y. Li, J. Shi, T. Tian, R. Jia and Y. Liu, *J. Alloys Compd.*, 2021, **875**, 159970.
38 T. Ma, F. Liang, R. Chen, S. Liu and H. Zhang, *Nanomaterials*, 2020, **124**(14), 7812–7822.
39 Y. Feng, X. Y. Yu and U. Paik, *Sci. Rep.*, 2016, **6**, 1–8.
40 Y. Ullal and A. C. Hegde, *Int. J. Hydrogen Energy*, 2014, **39**, 10485–10492.
41 H. Meng, Z. Ren, S. Du, J. Wu, X. Yang, Y. Xue and H. Fu, *Nanoscale*, 2018, **10**, 10971–10978.
42 M. H. Suliman, A. Adam, L. Li, Z. Tian, M. N. Siddiqui, Z. H. Yamani and M. Qamar, *ACS Sustain. Chem. Eng.*, 2019, **7**, 17671–17681.
43 M. Suliman, A. Al Ghamdi, T. Baroud, Q. Drmosh, M. Rafatullah, Z. Yamani and M. Qamar, *Int. J. Hydrogen Energy*, 2022, **47**, 23498–23507.
44 M. A. Ehsan, Z. Ullah, M. F. Nazar, M. Younas and M. Suliman, *Int. J. Hydrogen Energy*, 2023, **48**(42), 15784–15795.
45 L. Li, W. Huang, J. Lei, B. Shang, N. Li and F. Pan, *Appl. Surf. Sci.*, 2019, **479**, 540–547.
46 G. Zhang, J. Zeng, J. Yin, C. Zuo, P. Wen, H. Chen and Y. Qiu, *Appl. Catal., B*, 2021, **286**, 119902.
47 L. Wang, J. Geng, W. Wang, C. Yuan, L. Kuai and B. Geng, *Nano Res.*, 2015, **8**, 3815–3822.
48 Y. Li, L. Ge, Y. Zhou, L. Li, W. Li, J. Xu and Y. Li, *Inorg. Chem. Front.*, 2020, **7**, 4930–4938.
49 J. R. Swierk, S. Klaus, L. Trotochaud, A. T. Bell and T. D. Tilley, *J. Phys. Chem. C*, 2015, **119**, 19022–19029.
50 Y. Lin, S. Zhou, S. W. Sheehan and D. Wang, *J. Am. Chem. Soc.*, 2011, **133**, 2398–2401.
51 Y. Zhu, M. Jiang, M. Liu, L. Wu, G. Hou and Y. Tang, *Nanoscale*, 2020, **12**, 3803–3811.